Aberystwyth University

Late Holocene anti-phase change in the East Asian summer and winter monsoons

Kang, Shugang; Wang, Xulong; Roberts, H. M.; Duller, G. A. T.; Cheng, Peng; Lu, Yanchou; An, Zhisheng

Published in:
Quaternary Science Reviews

DOI:
10.1016/j.quascirev.2018.03.028

Publication date:
2018

Citation for published version (APA):
Kang, S., Wang, X., Roberts, H. M., Duller, G. A. T., Cheng, P., Lu, Y., & An, Z. (2018). Late Holocene anti-phase change in the East Asian summer and winter monsoons. *Quaternary Science Reviews*, *188*, 28-36. https://doi.org/10.1016/j.quascirev.2018.03.028

Kang, S., Wang, X.L., Roberts, H.M., Duller, G.A.T., Cheng, P., Lu, Y.C., and An, Z.S. (In Press, 2018) Late Holocene anti-phase change in the East Asian summer and winter monsoons. Quaternary Science Reviews
DOI: 10.1016/j.quascirev.2018.03.028

Late Holocene anti-phase change in the East Asian summer and winter monsoons

Shugang Kang [a, *], Xulong Wang [a], Helen M. Roberts [b], Geoff A. T. Duller [b], Peng Cheng [a], Yanchou Lu [a], Zhisheng An [a]

[a] State Key Laboratory of Loess and Quaternary Geology, Institute of Earth Environment, Chinese Academy of Sciences, Xi'an, 710061, China

[b] Department of Geography and Earth Sciences, Aberystwyth University, Aberystwyth, Ceredigion, SY23 3DB, UK

[*]e-mail: kshg@ieecas.cn (Shugang Kang)

Abstract

Changes in East Asian summer and winter monsoon intensity have played a pivotal role in the prosperity and decline of society in the past, and will be important for future climate scenarios. However, the phasing of changes in the intensity of East Asian summer and winter monsoons on millennial and centennial timescales during the Holocene is unclear, limiting our ability to understand the factors driving past and future changes in the monsoon system. Here, we present a high resolution (up to multidecadal) loess record for the last 3.3 ka from the southern Chinese Loess Plateau that clearly demonstrates the relationship between changes in the intensity of the East Asian summer and winter monsoons, particularly at multicentennial scales. At multimillennial scales, the East Asian summer monsoon shows a steady weakening, while the East Asian winter monsoon intensifies continuously. At multicentennial scales, a prominent ~700-800 yr cycle in the East Asian summer and winter monsoon intensity is observed, and here too the two monsoons are anti-phase. We conclude that multimillennial changes are driven by Northern Hemisphere summer insolation, while multicentennial changes can be correlated with solar activity and changing strength of the Atlantic meridional overturning circulation.

Key words: Holocene; Chinese loess; Quartz OSL; East Asian summer monsoon; East Asian winter monsoon; Insolation; Solar activity

1. Introduction

The East Asian monsoon system includes the warm-moist southeasterly East Asian summer monsoon (EASM) and the cold-dry northwesterly East Asian winter monsoon (EAWM) (Fig. 1a), which both show great variability at different timescales (e.g. orbital, millennial, centennial, decadal) and play a role in the development of the economy, society, biology etc. of East Asia (Wang, 2006). Changes in past EASM and/or EAWM intensity have been reconstructed from a variety of palaeoclimate archives, including loess (e.g. An et al., 1991a, 1991b; Ding et al., 2002; Hao et al., 2012; Sun et al., 2012; Lu et al., 2013; Xia et al., 2014; Li and Morrill, 2015), deserts (e.g. Yang et al., 2011; Yang et al., 2013; Long et al., 2017), lake sediments (e.g. Yancheva et al., 2007; Liu et al., 2009; An et al., 2012; Wang et al., 2012; Chen et al., 2015), cave speleothem (e.g. Wang et al., 2005; Wang et al., 2008; Zhang et al., 2008; Cheng et al., 2016), ocean sediments (e.g. Tian et al., 2010; Steinke et al., 2011; Zheng et al., 2014; Zhang et al., 2015) etc., which is important for the understanding of present and future monsoon climate (Wang, 2006). At present, it is widely accepted that the EASM and EAWM intensity are anti-phase at both orbital- and millennial-scales beyond the Holocene (e.g. during the last glacial-interglacial cycle), as is well documented by loess on the Chinese Loess Plateau (CLP) and cave speleothem in southern China (e.g. An et al., 1991a, 1991b; Ding et al., 2002; Wang et al., 2008; Hao et al., 2012; Sun et al., 2012; Cheng et al., 2016; Maher, 2016). Orbital-scale EASM and EAWM variability can be mainly attributed to changes in orbitally-induced

Northern Hemisphere summer insolation (NHSI) (Ding et al., 2002; Hao et al., 2012; Cheng et al., 2016), and changes of the Atlantic meridional overturning circulation (AMOC) strength are suggested to be potentially responsible for last glacial millennial-scale changes (Wang et al., 2008; Sun et al., 2012).

[Here, insert Fig. 1]

Although changes of the EASM intensity at various timescales during the Holocene have been well reconstructed (e.g. Wang et al., 2005; Zhang et al., 2008; Liu et al., 2009; Tan et al., 2011; An et al., 2012; Lu et al., 2013; Chen et al., 2015), EAWM records are still sparse. The existing EAWM records (e.g. Yancheva et al., 2007; Liu et al., 2009; Tian et al., 2010; Steinke et al., 2011; Wang et al., 2012; Xia et al., 2014; Zheng et al., 2014; Li and Morrill, 2015; Yan et al., 2015; Zhang et al., 2015; Wen et al., 2016) are mostly based on non-aeolian deposits and are always controversial. Great differences were observed in previous studies of EAWM intensity changes and forcing mechanisms during the Holocene, and relationships between EASM and EAWM have been variously described as in-phase, anti-phase and out-of-phase at different timescales. Thus, robust high-resolution EAWM records are required to understand the phase relationship between the EASM and EAWM and their forcing mechanisms.

When compared with other sediments, loess on the CLP provides advantages for exploring the phase relationship between EASM and EAWM. This is because the classic, widely-accepted (An et al., 1991a, 1991b; Ding et al., 2002; Hao et al., 2012; Sun et al., 2012; Lu et al., 2013; Xia et al., 2014; Li and Morrill, 2015; Maher, 2016) proxies used to infer the EASM (e.g. magnetic susceptibility (MS)) and EAWM (e.g. mean grain size (MGS)) intensity can synchronously record the intensity changes in both EASM and EAWM. However, there is still a lack of millennial- and centennial-scale EASM and EAWM records in Chinese loess during the Holocene (Lu et al., 2013; Xia et al., 2014; Li and Morrill, 2015), due to the typically low-resolution of records, coupled with limited chronology, possible disturbance by human beings, and biologic activities etc. (Stevens et al., 2006). The existing records show both in-phase (Li and Morrill, 2015) and out-of-phase (Xia et al., 2014) relationships, based on loess in the western and southern CLP respectively.

Reconstruction of past EASM and EAWM changes during the late Holocene (e.g. since ~ 3 ka) is particularly important for understanding short timescale (e.g. centennial, decadal) monsoons dynamics and is significant for prediction of monsoon changes in the future. Meanwhile, palaeomonsoon records are significant for interpreting evolution of human activity, culture etc. in East Asia. As mentioned above, during the late Holocene, the EASM intensity changes revealed from different archives are relatively clear, and the high-resolution EAWM records, particularly based on loess on the CLP, are difficult to achieve and are indeed needed. In this study, based on loess from the Weinan site at southern CLP, considering the dust accumulation rate (DAR) changes and loess resolution, we focus on the late Holocene (the last ~ 3.3 ka) record to reveal EASM and EAWM intensity changes, and their phases and dynamics at multimillennial- and multicentennial-scale.

2. Study area

Situated at the southern margin of the CLP, the Weinan loess section (WN2, 34º24'54.85"N, 109º33'44.18"E, 646 m a.s.l.) is located at the center of a flat tableland ("Dong Yuan" in Chinese), which is approximately 10 km from east to west and 20 km from south to north (Fig. S1b). To the south of the "Dong Yuan" is the Qinling Mountain, which is ~ 1500-m higher than the surface of "Dong Yuan", and to the north of it is the Guanzhong Basin, which is ~ 150-m lower than the surface of "Dong Yuan" (Fig. S1b). To the north of the Guanzhong Basin is the main body of the classic CLP (Fig. S1a). Previous studies have widely confirmed that loess around Weinan can be used to reconstruct past climate and environment changes at orbital- and millennial-scale during the Quaternary (e.g. Liu et al., 1994; Guo et al., 1996; Liu and Ding, 1998; Hao and Guo, 2005; Sun et al., 2010; Kang et al., 2013). However, there is still a lack of high-resolution Holocene records here.

The Weinan loess section in this study is about 600 km to the southeast of the landward limit of the modern EASM front (Fig. 1a). In addition, considering the decline of EASM intensity since the early or middle Holocene (Wang et al., 2005;

Wang et al., 2008; Lu et al., 2013; Chen et al., 2015), it is reasonable to say that, the Weinan Holocene loess section can be influenced by the EASM throughout the Holocene. Modern mean annual precipitation and temperature are 645 mm and 13.6 °C respectively at Weinan, with rainfall mainly occurring in summer, brought by EASM winds. During winter and spring, the weather here is generally cold and dry, influenced by the EAWM.

3. Material and methods

3.1. Site description and sampling

The Weinan loess outcrop (Figs. 1b and S2a) was made in a brickyard years ago. The boundary between the uppermost palaeosol (S0) and beneath typical loess (L1) is clear during the field observation. Based on the soil texture, soil color etc. (Figs. 1b, 1c and S2a), the Weinan loess outcrop can be divided into three parts, including typical loess (L1), a depth below 2.7 m, strongly-developed palaeosol (S0), a depth of ~ 2.7-1.2 m , and relatively weakly-developed palaeosol (L0), a depth above ~ 1.2 m. Specifically for loess from a depth of 1.9-0.0 m, focused upon in this study, the soil becomes gradually loose and changes from brownish to yellowish. In addition, there is a relatively strongly-developed palaeosol unit at a depth of 0.8-0.6 m.

Fig. 1b shows the weathered outcrop. To obtain fresh samples, a new 3.5-m pit was excavated at Weinan after removal of the uppermost ~ 20-cm severely-disturbed loess (Fig. 1c). Powder samples, used for MS and grain size analysis, were obtained at 2-cm intervals for depths above 3.2 m below the surface. Luminescence samples, used for fine-grained (4-11 μm) quartz optically stimulated luminescence (OSL) age determination, were collected at 10-20-cm intervals for depths from 3.1 to 0.1 m below the surface by hammering 20-cm-long, 5-cm-diameter stainless steel cylinders into the fresh section (Fig. 1c). In total, 161 powder samples and 19 luminescence samples were obtained.

3.2. Quartz OSL dating

The luminescence sample tubes were processed under subdued red light conditions in the luminescence laboratory. The sediments at both ends of the tube were removed, and the rest of the non-light exposed loess sample was prepared for quartz OSL equivalent dose (D_e) determination and for analysis of the radioisotope concentrations (ppm U, Th and % K). The samples (~ 50 g) were first treated with 30% w.w. H_2O_2 and 37% v.v. HCl to remove organic materials and carbonates, respectively. The samples were washed with distilled water until reaching pH neutral, and then 4-11 μm diameter polymineral grains were separated according to Stokes' law. These grains were immersed in 30% hydrofluorosilicic (H_2SiF_6) for 3-5 days to extract the fine-grained quartz component. The resultant fluoride was removed using 37% v.v. HCl. Finally, the purified quartz was deposited on 9.7-mm-diameter stainless steel discs using ethanol and dried prior to measurement. The purity of the extracted quartz was verified by examing the 110 °C (at 5 °C/s heating rate) thermoluminescence (TL) peak from quartz, the regenerative dose infrared stimulated luminescence (IRSL)

Kang, S., Wang, X.L., Roberts, H.M., Duller, G.A.T., Cheng, P., Lu, Y.C., and An, Z.S. (In Press, 2018) Late Holocene anti-phase change in the East Asian summer and winter monsoons. Quaternary Science Reviews
DOI: 10.1016/j.quascirev.2018.03.028

signal intensity, and the OSL IR depletion ratio (Duller, 2003; Fig. S3).

All of the OSL measurements were performed using an automated Daybreak 2200 OSL reader equipped with infrared (880±60 nm) and blue (470±5 nm) LED units and a $^{90}Sr/^{90}Y$ beta source for irradiation. The quartz grains were stimulated at 125 °C with blue LEDs (maximum power of ~ 45 mW•cm^{-2}) for 1 minute, and the OSL signal was detected using an EMI 9235QA photomultiplier tube filtered with two 3-mm thick U-340 (pass bands of ~ 290-370 nm) glass filters. The OSL signal used was obtained from the integral of the first 2-s of the decay curve minus the last 2-s. The quartz OSL D_e was determined using the single-aliquot regenerative-dose (SAR) protocol ((Murray and Wintle, 2000; Wintle and Murray, 2006), Section S1 and Table S1). According to the preheat plateau test results of sample WN2-50 (Fig. S5), temperatures of 260 ºC and 220 ºC for 10 s were used prior to measurement of the natural/regenerative-dose and the test dose OSL signals, respectively. Conventional checks in SAR protocol (Section S1), including tests of dose recovery, recycling ratio and recuperation ratio (Fig. S6), and the fine-grained quartz luminescence characteristics (e.g. dose-response curve, OSL signal decay curve, brightness; Fig. S7) suggest that it is reliable to date the Weinan loess by using this protocol. Details related to quartz OSL D_e determination are presented in Section S1.

For dose rate determination, U and Th concentration was measured using inductively coupled plasma mass spectrometry (ICP-MS), and X-ray fluorescence (XRF) was used to determine the K concentration. According to previously measured water contents since the last interglacial at a nearby (in several kilometers) site (Weinan, WN) (Kang et al., 2011, 2013), to account for the effect of water on dose rate, a water content of 20±5% (weight of water/weight of dry sediments) was assumed for all the luminescence samples. The fine-grained quartz α-value was assumed to be 0.04±0.002 (Rees-Jones, 1995). The cosmic dose rates were calculated using the equations of Prescott and Hutton (1988) and Prescott and Hutton (1994).

Finally, the quartz OSL ages (expressed in ka) are simply obtained through dividing the measured D_e (Gy) by the calculated environmental dose rate (Gy/ka).

3.3. Magnetic susceptibility and grain size measurements

Following oven-drying of samples, low-frequency MS was measured six times using a Bartington MS2 to obtain an average value. Prior to grain size distribution measurements, the organic matter and carbonate in samples were removed using H_2O_2 and HCl respectively. After dispersal with an ultrasonic bath containing 10 ml 10% $(NaPO_3)_6$ solution, the grain size distribution (e.g. Fig. S4) was measured using a Malvern 2000 laser instrument. Replicate measurements show that the MS and MGS have analytical errors of <1% and <2%, respectively.

3.4. Smoothing and detrending

For better comparison between different records, only data covering the late Holocene (the last ~ 3.3 ka, equal to the time length during the late Holocene at Weinan in this study) were used in all the mentioned data in this study. To reveal centennial- or smaller-scale climate change, long-term (greater than 1 ka) palaeoclimate variations should be removed. Palaeoclimate series without the same time-resolution were interpolated, with the interpolated time interval generally equal to corresponding original smallest time interval. Considering the high-resolution records used and the time-scale (multi-millennial and multi-centennial scales) focused upon this study, it is suggested that the interpolation is reasonable.

A 1-ka adjacent-averaging, non-weighted smoothing, was then applied to the interpolated or original palaeoclimate data, with the average value centered. Finally, the residual data were expressed as the interpolated or original data minus the smoothed data. This approach was applied to MS and MGS data from Weinan (Fig. S9; Details can be found from Section S2), and was also used for other palaeoclimate records mentioned in this study.

Thus, the residual palaeoclimate data covering the last ~ 3.3 ka, with identical time resolution, can also be used for periodicity analysis using the computer program Redfit35 (Schulz and Mudelsee, 2002). Considering the timescale focused upon in this study, only periodicity larger than 100 yrs was presented and considered here. Results of periodicity analysis was used to partly support the records correlation and mechanism explanation in our study.

4. Results and discussion

4.1. Chronology

The 19 quartz OSL ages (Table 1) are plotted against depth in Fig. 2c, which increase with depth, without reversals within errors, and indicate that the uppermost 3 m of loess at Weinan was deposited during the Holocene. There are 7 ages covering the early Holocene, ranging 12.02±0.77 to 7.28±0.47 ka, and 10 ages covering the late Holocene, changing from 3.48±0.22 to 0.21±0.01 ka, with a depth of 1.9-0.1 m. It seems that the middle Holocene loess is very thin (~ 20 cm in depth) in this section, and the dust accumulation is relatively fast during the late Holocene. In addition, considering the measured quartz OSL age changes with depth (Fig. 2c) and the field observation (Fig. S2), it is clear, the dust accumulation is continuous during the late Holocene at Weinan. Therefore, for high-resolution palaeoclimate reconstruction, the late Holocene deposition, is focused upon in this study.

[Here, insert Fig. 2]

To reconstruct past EASM and EAWM intensity changes and to compare them with other records, a continuous chronology throughout the late Holocene is needed. The 10 quartz OSL ages covering 190-10 cm were used in the Bayesian age-depth model in Bacon (Blaauw and Christen, 2011; Fig. S8d), which was run to achieve 2 cm final resolution. Results from Markov Chain Monte Carlo (MCMC) iterations, the distributions of accumulation rate prior and its memory (Fig. S8a-c) indicate the reliability of using the Bayesian age-depth model for the late Holocene loess chronology construction. And, chronology of a depth above 10 cm is obtained by linear extrapolation based on the Bayesian model ages at depths of 30 and 10 cm (Fig. 3c). Thus, the chronology covering the last ~ 3.3 ka at Weinan is established as shown in Fig. 3c. When used for climate change series reconstruction, the chronology from Bayesian model is corrected to ka BP.

[Here, insert Fig. 3]

4.2. Dust accumulation

Typically, the Holocene loess is ~ 1 m thick in the central and eastern part of the CLP, giving a mean DAR of ~ 1 cm/100 yrs (An, 2000; Kohfeld and Harrison, 2003; Yang et al., 2015). According to the quartz OSL dating results (Fig. 2c and Table 1), the Weinan late Holocene (the last ~ 3.3 ka) loess section, with thickness of ~ 1.9 m, shows fast dust accumulation, equal to mean DAR of ~ 6 cm/100 yrs (Fig. 5j), which is much higher than that at other typical sites on the CLP (Yang et al., 2015) and is even similar with some fast deposition sites at the western CLP (e.g. Chen et al., 1991). Temporally, the obvious increase in DAR during the late Holocene at Weinan can be partly attributed to the strong EAWM (Section 4.4).

Based on the north-south orientated outcrop (~ 400 m in width), made by a brickyard years ago, the Weinan Holocene loess becomes thicker and thicker from south to north, and reaches a stable level (thickness of ~ 3 m) from the middle part to the north most end of the outcrop (Fig. S2a and S2b). However, it is still unclear how far the stable outcrop can extend to the north. Considering the representativeness at a local scale, the sampling pit (Fig. 1c) is located at the northern part of the outcrop. It is suggested that, at the beginning of the Holocene, areas around the section showed relatively low geomorphology when compared with most of the other areas on "Dong Yuan". Therefore, areas around the section are more favorable for dust deposition and preservation, which finally lead to the high DAR during the early Holocene and particularly during the late Holocene (Fig. 2c). However, it is still clear that the middle Holocene palaeosol (depth of 2.1-1.9 m, ~ 7.3-3.3 ka BP) shows slow dust accumulation, equal to mean DAR of 0.5 cm/ 100 yrs. Here, we tentatively suggest that, the obvious reduction of dust material from deserts and the Gobi in northern and northwestern China, caused by the strong EASM-induced vegetation cover increase during the middle Holocene (Lu et al., 2013; Chen et al., 2015), may be the main reason. In addition, we did not find any erosion marks along the outcrop.

Field observation (e.g. soil texture, color) and the grain size distribution (Fig. S4) indicate the aeolian-formed nature of the late Holocene loess at Weinan. The dust source probably includes distal and local groups, with the distal component derived from the northern and northwestern arid areas (Liu and Ding, 1998), and the local component derived from the north and northwest to the section on "Dong Yuan" (Fig.

S1b). The distal and local components probably had almost the same age before deposition at the study section, both brought by the northwesterly EAWM winds. Thus, the late Holocene loess at the studied Weinan section amplifies the palaeoclimate signal, which leads to the potential of this late Holocene loess at recording centennial-scale, even decadal-scale, changes in EASM and EAWM intensity. Proxy samples, collected at 2-cm intervals, imply that the mean time-resolution of the Weinan site can be up to decades for the late Holocene. However, considering possible disturbance by biological activities etc., only climate signals beyond the decadal-scale (e.g. millennial and centennial scales) are discussed in this study.

4.3. Proxy and palaeoclimatic interpretation

4.3.1. Proxy records

The MS and MGS covering the uppermost 3.2 m are shown in Fig. 2a and 2b respectively, and those covering the uppermost 1.9 m were specifically shown in Fig. 3a and 3b respectively. It is clear that both MS and MGS show a long-term trend during the late Holocene at Weinan, with secondary fluctuations superimposed. The MS shows generally decreasing trend throughout the late Holocene, which is consistent with the observed pedogenesis change in the outcrop and in the fresh sampling pit. An obvious increase of MS can be found at a depth of ~ 0.8-0.6 m, equal to ~ 0.96-0.72 ka BP. The MGS results show that the loess generally becomes coarser and coarser since the late Holocene, and the secondary fluctuation is more obvious when compared with that of the MS data, such as the fining change at a depth of ~ 0.8-0.6 m.

To determine changes of MS and MGS at multicentennial-scale, after the measured MS and MGS were interpolated at the same temporal resolution, the interpolated data were smoothed and detrended using a 1 ka window (Sections 3.4 and S2). The residual MS (Δ MS) and MGS (Δ MGS), together with the measured data, are presented in Fig. 4. In this way, the short-term (e.g. multicentennial-scale) proxy changes can be well presented according to the residual data (Fig. 4b and 4c). Thus, the measured and residual MS and MGS can be used to evaluate both long-term (multimillennial-scale) and short-term (multicentennial-scale) palaeoclimate changes respectively. In addition, it is clear that variation in the magnitude of the residual MS and MGS is much larger than the corresponding analytical error, which ensures that the residual MS and MGS are reliable for expressing short-term changes.

[Here, insert Fig. 4]

4.3.2. Proxy interpretation

4.3.2.1. Magnetic susceptibility

In early studies, it was recognized that the bulk MS in palaeosols is several times higher than that in loess layers in Chinese loess (Heller and Liu, 1982; Kukla et al., 1988). Later, MS was suggested as an index of EASM intensity in Chinese loess (An et al., 1991a), which was widely accepted and has been used by the Quaternary community in past decades (Liu and Ding, 1998; An, 2000; Hao and Guo, 2005; Sun et al., 2010; Yang et al., 2015). Although, in the early studies of MS, concentration by decalcification and soil compaction processes (Heller and Liu, 1982) and the dilution effect (Kukla et al., 1988) were suggested to explain the enrichment of magnetic minerals, in recent decades, it has been widely accepted that MS enhancements are mainly related to the formation of fine-grained magnetic minerals (magnetite and maghemite), induced by pedogenic activity during warm and humid periods (Zhou et al., 1990; Maher and Thompson, 1991). Meanwhile, pedogenic intensity in Chinese loess is mainly controlled by EASM strength. When the EASM was strong, precipitation was high and plant cover is dense, which leads to intensified pedogenesis and a high proportion of ultrafine magnetic grains (An et al., 1991a). Therefore, the palaeosols in Chinese loess show high MS values. Conversely, when the EASM weakened, the climate was relatively dry and vegetation cover was relatively low, resulting in weakened pedogenesis and a decrease of magnetic minerals. Thus, relatively low MS values are found in loess layers (An et al., 1991a). Therefore, MS can be regarded as a reliable proxy of EASM intensity in Chinese loess.

4.3.2.2. Mean grain size

Spatially, the loess shows a fining trend from northwest to southeast on the CLP, and, specifically for some section, the grain size is larger in loess layers than that in palaeosols (Liu, 1985). The northwesterly winds are responsible for dust transport from the deserts and the Gobi in northern China to the CLP, and the loess deposition is thought to be largely controlled by the intensity of the EAWM during the cold season (An et al., 1991b). Thus, grain size distribution was favored as an effective proxy of EAWM intensity (An et al., 1991b; Xiao et al., 1995). Though different grain-size index(es) (e.g. mean grain size, median grain size, > 63 μm %) have been adopted over time, all the grain-size parameters show very similar patterns, which implies that no single grain-size parameter is critical as an indicator of EAWM intensity (Liu and Ding, 1998). In this study, the MGS is chosen as the proxy of EAWM intensity, with large (small) MGS indicating a strong (weak) EAWM. In addition, to some extend, DAR can also be used as a proxy of EAWM intensity, with high (low) DAR indicating strong (weak) EAWM (Liu and Ding, 1998; An, 2000).

4.4. Anti-phase changes in EASM and EAWM intensity

According to the raw data in Fig. 5a, 5j and 5k and the 1-ka smoothed data in Fig. S10a and S10k, at the multimillennial-scale, the EASM shows continuous weakening during the late Holocene, which can be well-correlated with other high-resolution EASM indices from adjacent areas, including records from Dongge Cave in southern China (Fig. 5b; Wang et al., 2005), Qinghai Lake in northwestern China (Fig. 5c; Sun et al., 2012), and particularly Gonghai Lake in northern-central China (Fig. 5d; Chen et al., 2015). In contrast, the EAWM is gradually strengthened, as indicated by MGS and DAR, which is generally consistent with records from Huguangyan Maar Lake in southern China (Fig. 5h; Yancheva et al., 2007) and the Okinawa Trough in the northwestern Pacific Ocean (Fig. 5i; Zheng et al., 2014). The anti-phase change between EASM and EAWM intensity at the multimillennial-scale can also be clearly revealed from the correlation analysis between MS and MGS at Weinan (Fig. 4e).

[Here, insert Fig. 5]

Compared with previous loess records on the CLP, the multimillennial-scale EASM and EAWM changes during the late Holocene reconstructed at Weinan are well consistent with those from the Yaoxian (YX) section (Xia et al., 2014), in which the pedogenic MS and the palaeorainfall are used to indicate the EASM intensity, and the grain size of > 30 μm (%) is chosen as a proxy of EAWM intensity. At the classic Luochuan loess section in the central CLP, the general decrease of EASM intensity during the late Holocene is also revealed according to the proxy of MS and $\delta^{13}C$ (Lu et al., 2013). The grain size (20-159 μm (%) and 20-200 μm (%)) based EAWM intensity at the Huangyanghe site on the northern foothill of Qilian Mountains (the western margin of CLP) shows a steadily increase trend during the late Holocene (Li and Morrill, 2014), which is consistent with the results from Weinan (this study) and Yaoxian (Xia et al., 2014). Thus, it seems that the EASM and EAWM intensity since at least the late Holocene revealed from loess on the CLP is similar. To our knowledge, our reconstruction of EASM and EAWM intensity at the multimillennial-scale during the late Holocene at Weinan is the most continuous on the CLP, with a reliable high-resolution chronology.

At the multicentennial-scale, both the EASM and EAWM intensity changes frequently at Weinan, with an opposing relationship and prominent ~ 700-800-yr cycle (Figs. 6a, 6j, 7 and S12). The anti-phase change between EASM and EAWM intensity at the multicentennial-scale can also be partly confirmed from the correlation analysis between Δ MS and Δ MGS at Weinan (Fig. 4f). Multicentennial-scale changes in EASM intensity at Weinan also can be correlated with records from Dongge cave (Fig. 6b; Wang et al., 2005), Gonghai Lake (Fig. 6d; Chen et al., 2015) and especially Qinghai Lake (Fig. 6c; An et al., 2012). Additionally, the EAWM records at Weinan are partly consistent with those from Huguangyan Maar Lake (Fig. 6i; Yancheva et al., 2007). Among the mentioned monsoon records in this study, only the EASM records from Qinghai Lake (Fig. 6c; An et al., 2012) and the EASM and EAWM records from Weinan show this prominent ~ 700-800-yr cycle (Figs. 7 and S12), which probably indicates that both the Weinan loess in this study and the Qinghai Lake sediments are sensitive to the ~ 700-800-yr cycle climate change. It is also clear that there is no obvious lead or lag between EASM and EAWM recorded by the Weinan loess.

[Here, insert Fig. 6]

[Here, insert Fig. 7]

Previously, the most detailed EASM and EAWM reconstruction using Chinese loess is at millennials scale during the last glacial (e.g. Sun et al., 2012). Here, we firstly show that Chinese loess has potential at recording much finer EASM and EAWM changes, such as the multicentennial-scale changes recorded at the Weinan section. Particularly, the EAWM records at multicentennial-scale here can be significant for recognition of EAWM changes and its dynamics in East Asia.

The Weinan loess-based monsoon records (Fig. 6a and 6j) are significant for palaeoclimate reconstruction during some notable multicentennial-scale events in the past ~ 3 ka in East Asia (e.g. LIA-Little Ice Age, corresponding to Bond 0 (Bond et al., 2001), MCA-Medieval Climate Anomaly, DACP-Dark Age Cold Period, corresponding to Bond 1 (Bond et al., 2001), RWP-Roman Warm Period, NP-Neoglacial Period). It is relatively warmer during the early NP (3.2-2.9 ka BP) than during the late NP (2.9-2.5 ka BP). It is relatively warm and humid during the early (2.50-1.90 ka BP) and late (1.65-1.30 ka BP) RWP, interrupted by a relatively cold period during the middle (1.90-1.65 ka BP) RWP. During the cold DACP (1.30-1.10 ka BP), the EAWM intensity stays at a high level. Warm and humid climate conditions dominate during the MCA (1.10-0.70 ka BP), brought about by the relatively strong EASM. Although the EAWM is strong during the early LIA (0.70-0.40 ka BP), with cold conditions, it is relatively weak during the late LIA (0.40-0.25 ka). Here, it is also clear that, the EASM and EAWM are anti-phase during the multicentennial-scale palaeoclimate events described above.

4.5. Insolation and solar activity impact on monsoon changes

According to the OSL-based high-resolution loess records at Weinan (Figs. 5a, 5k, 6a and 6j), EASM and EAWM intensity are anti-phase at both multimillennial- and multicentennial-scale during the late Holocene, without obvious leads or lags at multicentennial-scale, which implies a possible coherent forcing mechanism of changes in EASM and EAWM intensity.

In contrast to the EAWM, the continuous weakening of the EASM at a multimillennial-scale during the late Holocene follows the orbitally-induced decay of NHSI (Berger and Loutre, 1991) (Fig. 5), which is believed to be the driving factor of changes in EASM and EAWM intensity at the orbital-scale (Ding et al., 2002; Wang et al., 2008; Hao et al., 2012; Cheng et al., 2016). Here, we also suggest that changes in the EASM and EAWM at a multimillennial-scale during the late Holocene are controlled by NHSI, probably through the migration of annual mean position of the intertropical convergence zone (ITCZ) (Yancheva et al., 2007). The decreased NHSI and its induced Northern Hemisphere cooling can lead to the gradual southward shift of the mean annual position of the ITCZ throughout the late Holocene (Haug et al., 2001; Kobashi et al., 2013; Mohtadi et al., 2016), causing a decrease in EASM intensity (Fig. 5). Meanwhile, the meridional temperature gradient increase can lead to a strong EAWM (Fig. 5). Previous studies have shown both an in-phase and a lagged relationship of the EASM with NHSI (Wang et al., 2005; Lu et al., 2013; Chen et al., 2015). However, due to limitations of the temporal extent of the records, it is impossible to determine the synchronization between EASM/EAWM and NHSI based on the Weinan late Holocene records..

At a multicentennial-scale, changes in residual MS and residual MGS from Weinan loess can be well-correlated with the atmospheric residual ^{14}C ($\Delta\,^{14}C$) (Reimer et al., 2013) (Figs. 6 and S11), where higher (lower) values represent weak (strong) solar activity, and also with the North Atlantic residual hematite-stained grains (% HSG). Periodicity analysis further confirms this relationship, as shown by the similar ~700-800-yr cycle between Δ MS, Δ MGS, $\Delta\,^{14}C$ and Δ HSG (Figs. 7 and S12).

Thus, as previously suggested (Wang et al., 2005; Zhang et al., 2008; Liu et al., 2009; An et al., 2012), the correlation and spectral analysis results (Figs. 6 and 7) discussed in the present study suggest a potential link between solar activity and EASM and EAWM intensity. Previous studies also indicate that the ~ 1500-yr periodicity of climate change in the North Atlantic region during the last glacial and the Holocene probably originates from variations in solar activity (Bond et al., 2001). Although changes in solar output are rather small at multicentennial-scale during the late Holocene, nonlinear responses and feedback processes (e.g. “top-down”, “bottom-up” (Mohtadi et al., 2016)) may amplify the solar output effect. It is clear that the Northern Hemisphere temperature changes in a similar pattern with solar activity at multi-centennial scale during the late Holocene (Fig. 5e). Here, we propose that the solar activity-induced shift of the annual mean position of ITCZ possibly controls the changes in EASM and EAWM intensity. For example, when solar activity is weak, the Northern Hemisphere becomes cooler and the annual mean position of ITCZ shifts southward, which leads to a weak EASM and a strong EAWM.

The similarity between multicentennial-scale variations of EASM (Fig. 6a) and EAWM (Fig. 6j) and ice drift in North Atlantic (Fig. 6h), which is suggested to be probably forced also by solar activity (Bond et al., 2001), suggest that AMOC can affect the EASM and EAWM possibly through atmospheric and oceanic circulation (e.g. the westerlies) and redistribution of the annual mean position of the ITCZ (Haug et al., 2001; Wang et al., 2005; Sun et al., 2012). A slow-down of AMOC can lead to cooling in the North Atlantic area and an increased meridional temperature gradient in Northern Hemisphere mid-latitudes (Sun et al., 2012) and a southward shift of mean annual position of the ITCZ (Haug et al., 2001). Thus, the EASM is weakened and the EAWM is strengthened. In addition, the controlling influence of AMOC on the EASM and EAWM intensity can be further supported by the ~ 700-yr cycle of climate change, found from wavelet analysis of the sortable silt-size time-series data (a direct proxy for the North Atlantic THC/AMOC) from the NEAP-15 K core in North Atlantic (Dima and Lohmann, 2009; Soon et al., 2014), which is similar to the notable ~ 700-800-yr cycle EASM and EAWM changes recorded in the Weinan loess (Figs. 6 and 7).

5. Conclusions

Based on the high-resolution quartz OSL dating and the proxy results from magnetic susceptibility and mean grain size, we reconstruct the anti-phase change in the EASM and EAWM intensity based on Chinese loess at both multimillennial-scale and particularly multicentennial-scale during the late Holocene. At multimillennial scales, the EASM shows a steady weakening, while the EAWM intensifies continuously. For the first time, we reconstruct the EASM and EAWM multicentennial-scale changes based on the Chinese loess. At multicentennial scales, a prominent ~700-800 yr cycle in the EASM and EAWM intensity is observed. Our results suggest that Northern Hemisphere summer insolation controls multimillennial-scale change, and that solar activity and AMOC contribute to multi-centennial-scale change in the EASM and EAWM intensity during the late Holocene.

The reconstruction and the dynamic analysis presented in this study can contribute to the understanding of the role of climate change in economic and societal development, including the contribution to dynasty development and replacement in China, and is also important for evaluating past Asian-sourced dust activity and for predicting changes in EASM and EAWM intensity under the natural climate change scenarios, including through use of modelling approaches. Future work is needed to extend the EASM and EAWM records at multicentennial scales to longer time scales (e.g. covering the entire Holocene period) using Chinese loess.

Acknowledgements

We would like to thank Prof. Ana Moreno Caballud and the two anonymous reviewers for their constructive suggestions and comments. This study was supported by National Natural Science Foundation of China (41290254), National Key Research and Development Program of China (2016YFA0601902), Chinese Academy of Sciences (Youth Innovation Promotion Association) and State Key Laboratory of Loess and Quaternary Geology.

Figure legends

Figure 1 Site locations and Weinan loess section. (a) Location of Weinan section (this study) and other sites mentioned in the text, and atmospheric circulation in East Asia. QH-Qinghai (An et al., 2012), GH-Gonghai (Chen et al., 2015), DA-Dongge (Wang et al., 2005), HGY-Huguangyan (Yancheva et al., 2007), Oki02-Okinawa02 (Zheng et al., 2014), WN2-Weinan (this study), EASM-East Asian summer monsoon, EAWM-East Asian winter monsoon, CLP-Chinese Loess Plateau, TP-Tibetan Plateau. The white dashed line is the landward limit of the modern EASM front. The map is redrawn from Mapworld (http://en.tianditu.com/). (b) Weinan section weathered outcrop. (c) Fresh sampling pit at Weinan, with depth and stratigraphic division also indicated. The white dashed lines are the boundaries of L1/S0 and S0/L0. The uppermost 190-cm loess is focused upon in this study.

Figure 2 Stratigraphic division (the leftmost two columns), same as that in Figs. 1c and S2, and plots of magnetic susceptibility (MS) (a), mean grain size (MGS) (b) and optically stimulated luminescence (OSL) ages (in ka) (c) against depth at the Weinan site. The asterisk between the sampling pit picture and the sketch of the strata indicates that the loess color was caused by heavy rainfall before sampling in summer, as described in the caption to Fig. S2. Original numerical data in this figure can be found in Supplementary Data.

Figure 3 Stratigraphy, proxy (MS and MGS) and chronology for the uppermost 190 cm loess at Weinan, same as those in Fig. 2. Quartz OSL ages in (c) are fitted by the Bayesian age-depth model using Bacon (Blaauw and Christen, 2011; Fig. S8). The black solid line in (c) shows the constructed chronology. The asterisk at the leftmost column is the same as that in Fig. 2. Original numerical data in this figure can be found in Supplementary Data.

Figure 4 Measured magnetic susceptibility (MS) (a), measured mean grain size (MGS) (h) and their correlation analysis (e), and residual MS (Δ MS) (b), residual MGS (Δ MGS) (c) and their correlation analysis (f) at Weinan in this study. Original numerical data in this figure can be found in Supplementary Data.

Figure 5 Late Holocene millennial-scale changes of EASM and EAWM intensity and related dynamic records. (a) Magnetic susceptibility (MS) and OSL ages (corrected to ka BP) at Weinan. (b) Dongge Cave $\delta^{18}O$ (Wang et al., 2005), relative to Vienna PeeDee Belemnite (VPDB) standard. (c) Qinghai Lake Asian summer monsoon index (SMI) (An et al., 2012). (d) Gonghai Lake reconstructed precipitation (Chen et al., 2015). (e) Northern high latitude (NHL) temperature anomaly (Kobashi et al., 2013). (f) Ti content of ODP1002 sediments from the Cariaco Basin (Haug et al., 2001). (g) Northern Hemisphere July solar insolation (Berger and Loutre, 1991). (h) Ti content of sediments from Huguangyan Maar Lake (Yancheva et al., 2007). (i) Grain size index (GSI) of Oki02 sediments from the Okinawa Trough (Zheng et al., 2014). (j)

Dust accumulation rate (DAR) calculated based on the Bayesian age-depth model fitted chronology (Fig. 4c) and, (k) Mean grain size (MGS) at Weinan in this study. Original numerical data in this figure can be found in Supplementary Data.

Figure 6 Late Holocene centennial-scale change in EASM and EAWM intensity and related dynamic records. (a) Weinan residual MS and OSL ages (corrected to ka BP). (b) Dongge Cave residual $\delta^{18}O$ (Wang et al., 2005), relative to VPDB standard. (c) Qinghai Lake residual SMI (An et al., 2012). (d) Gonghai Lake residual precipitation (Chen et al., 2015). (e) Northern Hemisphere residual temperature anomaly (Kobashi et al., 2013). (f) Atmospheric residual ^{14}C (Reimer et al., 2013). (g) Cariaco Basin residual Ti (Haug et al., 2001). (h) North Atlantic residual HSG (Bond et al., 2001). (i) Huguangyan Maar Lake residual Ti (Yancheva et al., 2007). (j) Weinan residual MGS. The pink and blue bands indicate strong (weak) EASM (EAWM) and strong (weak) EAWM (EASM) respectively. Signals larger than 1 ka are all filtered. Several climate periods are listed in the rightmost column. Original numerical data in this figure can be found in Supplementary Data.

Figure 7 Periodicity analysis of Δ MS (a) and Δ MGS (b) of Weinan loess, atmospheric $\Delta\,^{14}C$ (Reimer et al., 2013) (c) and North Atlantic Δ %HSG (Bond et al., 2001) for the last 3.3 ka using redfit35 (Schulz and Mudelsee, 2002), which were calculated based on data in Fig. 6a, f, h, j. The blue curve indicates the spectrum density, and the red one indicates the 90% confidence level in each figure. The yellow vertical bands were placed according to the most significant cycle in Δ MS (667 yr), Δ MGS (833 yr), Δ ^{14}C (800 yr) and Δ HSG (858 yr). Only frequency lower than 10, equal to 100 yr, was plotted here. Original numerical data in this figure can be found in Supplementary Data.

References

An, Z., Kukla, G.J., Porter, S.C., Xiao, J., 1991a. Magnetic susceptibility evidence of monsoon variation on the Loess Plateau of central China during the last 130,000 years. Quat. Res. 36, 29-36.

An, Z.S., 2000. The history and variability of the East Asian paleomonsoon climate. Quat. Sci. Rev. 19, 171-187.

An, Z.S., Colman, S.M., Zhou, W.J., Li, X.Q., Brown, E.T., Jull, A.J.T., Cai, Y.J., Huang, Y.S., Lu, X.F., Chang, H., Song, Y.G., Sun, Y.B., Xu, H., Liu, W.G., Jin, Z.D., Liu, X.D., Cheng, P., Liu, Y., Ai, L., Li, X.Z., Liu, X.J., Yan, L.B., Shi, Z.G., Wang, X.L., Wu, F., Qiang, X.K., Dong, J.B., Lu, F.Y., Xu, X.W., 2012. Interplay between the Westerlies and Asian monsoon recorded in Lake Qinghai sediments since 32 ka. Sci Rep 2, 619.

An, Z.S., Kukla, G., Porter, S.C., Xiao, J.L., 1991b. Late Quaternary dust flow on the Chinese Loess Plateau. Catena 18, 125-132.

Berger, A., Loutre, M.-F., 1991. Insolation values for the climate of the last 10 million years. Quat. Sci. Rev. 10, 297-317.

Blaauw, M., Christen, J.A., 2011. Flexible paleoclimate age-depth models using an autoregressive gamma process. Bayesian Analysis 6, 457-474.

Bond, G., Kromer, B., Beer, J., Muscheler, R., Evans, M.N., Showers, W., Hoffmann, S., Lotti-Bond, R., Hajdas, I., Bonani, G., 2001. Persistent solar influence on North Atlantic climate during the Holocene. Science 294, 2130-2136.

Chen, F.H., Li, J.J., Zhang, W.X., 1991. Loess stratigraphy of the Lanzhou profile and its comparison with deep-sea sediment and ice core record. GeoJournal 24, 201-209.

Chen, F., Xu, Q., Chen, J., Birks, H.J.B., Liu, J., Zhang, S., Jin, L., An, C., Telford, R.J., Cao, X., Wang, Z., Zhang, X., Selvaraj, K., Lu, H., Li, Y., Zheng, Z., Wang, H., Zhou, A., Dong, G., Zhang, J., Huang, X., Bloemendal, J., Rao, Z., 2015. East Asian summer monsoon precipitation variability since the last deglaciation. Sci Rep 5, 11186.

Cheng, H., Edwards, R.L., Sinha, A., Spotl, C., Yi, L., Chen, S.T., Kelly, M., Kathayat, G., Wang, X.F., Li, X.L., Kong, X.G., Wang, Y.J., Ning, Y.F., Zhang, H.W., 2016. The Asian monsoon over the past 640,000 years and ice age terminations. Nature 534, 640-+.

Dima, M., Lohmann, G., 2009. Conceptual model for millennial climate variability: a possible combined solar-thermohaline circulation origin for the 1,500-year cycle. Climate Dynamics 32, 301-311.

Ding, Z.L., Derbyshire, E., Yang, S.L., Yu, Z.W., Xiong, S.F., Liu, T.S., 2002. Stacked 2.6-Ma grain size record from the Chinese loess based on five sections and correlation with the deep-sea $\delta^{18}O$ record. Paleoceanography 17, 1-21.

Duller, G., 2003. Distinguishing quartz and feldspar in single grain luminescence measurements. Radiat Meas 37, 161-165.

Guo, Z., Liu, T., Guiot, J., Wu, N., Lü, H., Han, J., Liu, J., Gu, Z., 1996. High frequency pulses of East Asian monsoon climate in the last two glaciations: link with the North Atlantic. Climate Dynamics 12, 701-709.

Hao, Q.Z., Guo, Z.T., 2005. Spatial variations of magnetic susceptibility of Chinese loess for the last 600 kyr: Implications for monsoon evolution. J. Geophys. Res.-Solid Earth 110, B12101.

Hao, Q.Z., Wang, L., Oldfield, F., Peng, S.Z., Qin, L., Song, Y., Xu, B., Qiao, Y.S., Bloemendal, J., Guo, Z.T., 2012. Delayed build-up of Arctic ice sheets during 400,000-year minima in insolation variability. Nature 490, 393-396.

Haug, G.H., Hughen, K.A., Sigman, D.M., Peterson, L.C., Röhl, U., 2001. Southward migration of the intertropical convergence zone through the Holocene. Science 293, 1304-1308.

Heller, F., Liu, T.S., 1982. Magnetostratigraphical dating of loess deposits in China. Nature 300, 431-433.

Kang, S., Wang, X., Lu, Y., 2013. Quartz OSL chronology and dust accumulation rate changes since the Last Glacial at Weinan on the southeastern Chinese Loess Plateau. Boreas 42, 815-829.

Kang, S.G., Lu, Y.C., Wang, X.L., 2011. Closely-spaced recuperated OSL dating of the last interglacial paleosol in the southeastern margin of the Chinese Loess Plateau. Quat. Geochronol. 6, 480-490.

Kobashi, T., Goto-Azuma, K., Box, J., Gao, C.-C., Nakaegawa, T., 2013. Causes of Greenland temperature variability over the past 4000 yr: implications for northern hemispheric temperature changes. Clim. Past. 9, 2299-2317.

Kohfeld, K.E., Harrison, S.P., 2003. Glacial-interglacial changes in dust deposition on the Chinese Loess Plateau. Quat. Sci. Rev. 22, 1859-1878.

Kukla, G., Heller, F., Liu, X.M., Xu, T.C., Liu, T.S., An, Z.S., 1988. Pleistocene climates in China dated by magnetic susceptibility. Geology 16, 811-814.

Li, Y., Morrill, C., 2015. A Holocene East Asian winter monsoon record at the southern edge of the Gobi Desert and its comparison with a transient simulation. Climate Dynamics 45, 1219-1234.

Liu, J.Q., Chen, T.M., Nie, G.Z., Song, C.Y., Guo, Z.T., Li, K., Gao, S.J., Qiao, Y.L., Ma, Z.B., 1994. Dating and reconstruction of the high resolution time series in the Weinan loess section of the last 150 000 years. Quaternary Sciences, 193-202 (in Chinese with English abstract).

Liu, T.S., 1985. Loess and the Environment. China Ocean Press, Beijing.

Liu, T.S., Ding, Z.L., 1998. Chinese loess and the paleomonsoon. Annu. Rev. Earth Planet. Sci. 26, 111-145.

Liu, X., Dong, H., Yang, X., Herzschuh, U., Zhang, E., Stuut, J.-B.W., Wang, Y., 2009. Late Holocene forcing of the Asian winter and summer monsoon as evidenced by proxy records from the northern Qinghai-Tibetan Plateau. Earth Planet. Sci. Lett. 280, 276-284.

Long, H., Shen, J., Chen, J.H., Tsukamoto, S., Yang, L.H., Cheng, H.Y., Frechen, M., 2017. Holocene moisture variations over the arid central Asia revealed by a comprehensive sand-dune record from the central Tian Shan, NW China. Quat. Sci. Rev. 174, 13-32.

Lu, H., Yi, S., Liu, Z., Mason, J.A., Jiang, D., Cheng, J., Stevens, T., Xu, Z., Zhang, E., Jin, L., 2013. Variation of East Asian monsoon precipitation during the past 21 ky and potential CO2 forcing. Geology 41, 1023-1026.

Maher, B.A., 2016. Palaeoclimatic records of the loess/palaeosol sequences of the Chinese Loess Plateau. Quat. Sci. Rev. 154, 23-84.

Maher, B.A., Thompson, R., 1991. Mineral magnetic record of the Chinese loess and paleosols. Geology 19, 3-6.

Mohtadi, M., Prange, M., Steinke, S., 2016. Palaeoclimatic insights into forcing and response of monsoon rainfall. Nature 533, 191-199.

Murray, A.S., Wintle, A.G., 2000. Luminescence dating of quartz using an improved single-aliquot regenerative-dose protocol. Radiat Meas 32, 57-73.

Prescott, J., Hutton, J., 1988. Cosmic ray and gamma ray dosimetry for TL and ESR. International Journal of Radiation Applications and Instrumentation. Part D. Nuclear Tracks and Radiation Measurements 14, 223-227.

Prescott, J.R., Hutton, J.T., 1994. Cosmic ray contributions to dose rates for luminescence and ESR dating: large depths and long-term time variations. Radiat Meas 23, 497-500.

Rees-Jones, J., 1995. Optical dating of young sediments using fine-grain quartz. Ancient TL 13, 9-14.

Reimer, P.J., Bard, E., Bayliss, A., Beck, J.W., Blackwell, P.G., Bronk Ramsey, C., Buck, C.E., Cheng, H., Edwards, R.L., Friedrich, M., 2013. IntCal13 and Marine13 radiocarbon age calibration curves 0-50,000 years cal BP. Radiocarbon 55, 1869-1887.

Schulz, M., Mudelsee, M., 2002. REDFIT: estimating red-noise spectra directly from unevenly spaced paleoclimatic time series. Computers & Geosciences 28, 421-426.

Soon, W., Herrera, V.M.V., Selvaraj, K., Traversi, R., Usoskin, I., Chen, C.T.A., Lou, J.Y., Kao, S.J., Carter, R.M., Pipin, V., Severi, M., Becagli, S., 2014. A review of Holocene solar-linked climatic variation on centennial to millennial timescales: Physical processes, interpretative frameworks and a new multiple cross-wavelet transform algorithm. Earth-Sci. Rev. 134, 1-15.

Steinke, S., Glatz, C., Mohtadi, M., Groeneveld, J., Li, Q.Y., Jian, Z.M., 2011. Past dynamics of the East Asian monsoon: No inverse behaviour between the summer and winter monsoon during the Holocene. Glob. Planet. Change 78, 170-177.

Stevens, T., Armitage, S.J., Lu, H.Y., Thomas, D.S.G., 2006. Sedimentation and diagenesis of Chinese loess: Implications for the preservation of continuous, high-resolution climate records. Geology 34, 849-852.

Sun, Y.B., Clemens, S.C., Morrill, C., Lin, X.P., Wang, X.L., An, Z.S., 2012. Influence of Atlantic meridional overturning circulation on the East Asian winter monsoon. Nat. Geosci. 5, 46-49.

Sun, Y.B., Wang, X.L., Liu, Q.S., Clemens, S.C., 2010. Impacts of post-depositional processes on rapid monsoon signals recorded by the last glacial loess deposits of northern China. Earth Planet. Sci. Lett. 289, 171-179.

Tan, L., Cai, Y., An, Z., Edwards, R.L., Cheng, H., Shen, C.-C., Zhang, H., 2011. Centennial-to decadal-scale monsoon precipitation variability in the semi-humid region, northern China during the last 1860 years: Records from stalagmites in Huangye Cave. Holocene 21, 287-296.

Tian, J., Huang, E.Q., Pak, D.K., 2010. East Asian winter monsoon variability over the last glacial cycle: Insights from a latitudinal sea-surface temperature gradient across the South China Sea. Paleogeogr. Paleoclimatol. Paleoecol. 292, 319-324.

Wang, B., 2006. The asian monsoon. Springer Science & Business Media.

Wang, L., Li, J.J., Lu, H.Y., Gu, Z.Y., Rioual, P., Hao, Q.Z., Mackay, A.W., Jiang, W.Y., Cai, B.G., Xu, B., Han, J.T., Chu, G.Q., 2012. The East Asian winter monsoon over the last 15,000 years: its links to high-latitudes and tropical climate systems and complex correlation to the summer monsoon. Quat. Sci. Rev. 32, 131-142.

Wang, Y., Cheng, H., Edwards, R.L., He, Y., Kong, X., An, Z., Wu, J., Kelly, M.J., Dykoski, C.A., Li, X., 2005. The Holocene Asian monsoon: links to solar changes and North Atlantic climate. Science 308, 854-857.

Wang, Y.J., Cheng, H., Edwards, R.L., Kong, X.G., Shao, X.H., Chen, S.T., Wu, J.Y., Jiang, X.Y., Wang, X.F., An, Z.S., 2008. Millennial- and orbital-scale changes in the East Asian monsoon over the past 224,000 years. Nature 451, 1090-1093.

Wen, X.Y., Liu, Z.Y., Wang, S.W., Cheng, J., Zhu, J., 2016. Correlation and anti-correlation of the East Asian summer and winter monsoons during the last 21,000 years. Nat. Commun. 7, 7.

Wintle, A.G., Murray, A.S., 2006. A review of quartz optically stimulated luminescence characteristics and their relevance in single-aliquot regeneration dating protocols. Radiat Meas 41, 369-391.

Xia, D., Jia, J., Li, G., Zhao, S., Wei, H., Chen, F., 2014. Out-of-phase evolution between summer and winter East Asian monsoons during the Holocene as recorded by Chinese loess deposits. Quat. Res. 81, 500-507.

Xiao, J., Porter, S.C., An, Z., Kumai, H., Yoshikawa, S., 1995. Grain size of quartz as an indicator of winter monsoon strength on the Loess Plateau of central China during the last 130,000 yr. Quat. Res. 43, 22-29.

Yan, H., Soon, W., Wang, Y., 2015. A composite sea surface temperature record of the northern South China Sea for the past 2500 years: A unique look into seasonality and seasonal climate changes during warm and cold periods. Earth-Sci. Rev. 141, 122-135.

Yancheva, G., Nowaczyk, N.R., Mingram, J., Dulski, P., Schettler, G., Negendank, J.F.W., Liu, J., Sigman, D.M., Peterson, L.C., Haug, G.H., 2007. Influence of the intertropical convergence zone on the East Asian monsoon. Nature 445, 74-77.

Yang, S.L., Ding, Z.L., Li, Y.Y., Wang, X., Jiang, W.Y., Huang, X.F., 2015. Warming-induced northwestward migration of the East Asian monsoon rain belt from the Last Glacial Maximum to the mid-Holocene. Proc. Natl. Acad. Sci. U. S. A. 112, 13178-13183.

Yang, X., Scuderi, L., Paillou, P., Liu, Z., Li, H., Ren, X., 2011. Quaternary environmental changes in the drylands of China–a critical review. Quat. Sci. Rev. 30, 3219-3233.

Yang, X., Wang, X., Liu, Z., Li, H., Ren, X., Zhang, D., Ma, Z., Rioual, P., Jin, X., Scuderi, L., 2013. Initiation and variation of the dune fields in semi-arid China–with a special reference to the Hunshandake Sandy Land, Inner Mongolia. Quat. Sci. Rev. 78, 369-380.

Zhang, P., Cheng, H., Edwards, R.L., Chen, F., Wang, Y., Yang, X., Liu, J., Tan, M., Wang, X., Liu, J., An, C., Dai, Z., Zhou, J., Zhang, D., Jia, J., Jin, L., Johnson, K.R., 2008. A Test of Climate, Sun, and Culture Relationships from an 1810-Year Chinese Cave Record. Science 322, 940-942.

Zhang, X.J., Jin, L.Y., Li, N., 2015. Asynchronous variation in the East Asian winter monsoon during the Holocene. J. Geophys. Res.-Atmos. 120, 5357-5370.

Zheng, X., Li, A., Wan, S., Jiang, F., Kao, S.J., Johnson, C., 2014. ITCZ and ENSO pacing on East Asian winter monsoon variation during the Holocene: Sedimentological evidence from the Okinawa Trough. Journal of Geophysical Research: Oceans 119, 4410-4429.

Zhou, L.P., Oldfield, F., Wintle, A.G., Robinson, S.G., Wang, J.T., 1990. Partly pedogenic origin of magnetic variations in Chinese loess. Nature 346, 737-739.

Supplementary Information

Late Holocene anti-phase change in the East Asian summer and winter monsoons

Shugang Kang [a, *], Xulong Wang [a], Helen M. Roberts [b], Geoff A. T. Duller [b], Peng Cheng [a], Yanchou Lu [a], Zhisheng An [a]

[a] State Key Laboratory of Loess and Quaternary Geology, Institute of Earth Environment, Chinese Academy of Sciences, Xi'an, 710061, China

[b] Department of Geography and Earth Sciences, Aberystwyth University, Aberystwyth, Ceredigion, SY23 3DB, UK

[*] e-mail: kshg@ieecas.cn (Shugang Kang)

1. Quartz OSL equivalent dose determination

The quartz single-aliquot regenerative-dose (SAR) optically stimulated luminescence (OSL) dating protocol, as presented in Table S1, was used for equivalent dose (D_e) measurement. Preheat temperatures of 260 ºC and 220 ºC for 10 s were used prior to measurement of the natural/regenerative-dose and the test dose OSL signals, respectively (see below for preheat plateau test). To remove OSL signal buildup during cycles of irradiation, preheat and stimulation, an optical stimulation at 280 ºC for 60 s (step 7 in Table S1) was applied at the end of each measurement cycle. To assess the reliability of the sensitivity changes corrected by the OSL signal from the test dose (step 4 in Table S1), OSL measurements of two repeated regenerative doses, the smallest (zero excluded) and the largest ones, were added after the dose-response curve construction.

A preheat plateau test (Fig. S5) was performed on sample WN2-50, which had a D_e value of ~ 2.14 Gy (Table 1). The results indicate that a wide preheat plateau exists for both the natural/regenerative dose (210-290 ºC, Fig. S5a) and the test dose (180-240 ºC, Fig. S5e). In addition, the conventional tests of recycling ratio, recuperation ratio and dose recovery ratio (Fig. S5b-d and f-h) all satisfy the criteria of the SAR protocol in the above two plateaus. Thus, in this study, a preheat temperature of 260 ºC and 220 ºC for 10 s was chosen for the natural/regenerative dose and the test dose, respectively (Table S1).

A dose recovery test was applied to 6 of the 19 samples (Fig. S6a). After the natural OSL signal was stimulated at 125 ºC for 120 s, each sample was given a radiation dose, close in value to the corresponding D_e value. Then, the laboratory given dose was measured using the SAR protocol (Table S1). The dose recovery ratios (recovered/given) are all found to be within ±10% of unity for the 6 samples (Fig. S6a). The recycling ratios (repeated/regenerative) are also within ±10% of unity for all 19 samples (Fig. S6b), which suggests that the OSL signal from the test dose (step 6 in Table S1) can correct for sensitivity changes. The recuperation ratios ((L0/T0)/(LN/TN)) are all less than 1% for all of the 19 samples (Fig. S6c), which demonstrate the negligible thermal transfer of charge during OSL measurements.

For D_e determination, sample WN2-50 was chosen as an example here. The natural and regenerative-dose quartz OSL decay curves for sample WN2-50 are plotted in Fig. S7a, which indicate that the quartz brightness is sufficient for OSL measurements. It is also clear that the OSL signal decays rapidly, with the OSL intensity reaching near-background levels in less than 10 s. After measurement of the natural OSL signal, typically, seven regenerative doses (including zero) which bracket the natural dose, were applied to each aliquot to construct a dose-response curve. The dose-response curve can be well described by a constant plus single saturating exponential function, as shown in Fig. S7b. The error on a single D_e value for an aliquot is derived according to the curve fitting method in Duller (2007), and the standard error of the mean D_e values was estimated from the D_e distribution of a set of aliquots. D_e values from 20 aliquots are shown in Fig. S7c as a radial plot, and in Fig. S7d as a probability density plot. We can see that the D_e distribution of sample WN2-50 is of high precision and low relative error, which finally leads to a mean D_e of 2.14±0.09 Gy. This implies that a limited number of aliquots (e.g. 5) are adequate for D_e determination. Thus, considering the homogeneity of aeolian loess, the mean D_e value of ~ 10 aliquots for each sample was used to determine the final D_e value. Finally, D_e values for the 19 samples were obtained, ranging from 0.79±0.03 to 50.52±2.03 Gy (Table 1). The D_e values show an increasing trend with depth.

2. Detrending of records from Weinan and from other mentioned sites

The original magnetic susceptibility (MS) data spanning the last 3.3 ka (Figs. 4a, 5a and S9a), depth from 1.9 to 0.0 m, contains 96 points, with the smallest time interval being 0.013 ka. The original MS data was then interpolated at the same time interval of 0.013 ka (Fig. S9b). Thus, there are 250 MS points. It is clear that the original and interpolated MS curves are nearly the same (Fig. S9a and S9b). To obtain millennial and centennial-scale changes, the interpolated MS data were first smoothed at a 1-ka window, equal to 77-point smoothing (Fig. S9c). Finally, the residual MS (Δ MS) data were obtained through the interpolated MS minus the smoothed MS (Figs. 4b, 6a and S9d). The Δ MS record can be used to present centennial- or smaller-scale changes. All the raw data in Fig. 5 except that in Fig. 5g, 5i and 5j were handled as the MS data. Then, the 1-ka smoothed and detrended data were obtained (Figs. 6 and S9).

Supplementary tables

Table S1 Quartz single-aliquot regenerative-dose (SAR) optically stimulated luminescence (OSL) equivalent dose (D_e) determination protocol used for Weinan Holocene loess in this study, modified from Murray and Wintle (2000) and Wintle and Murray (2006).

Step	Treatment	Observed
1	Give dose, D_i	-
2	Preheat to 260 ºC for 10 s	-
3	OSL for 60 s at 125 ºC	L_i
4	Give test dose, D_t	-
5	Preheat to 220 ºC for 10 s	-
6	OSL for 60 s at 125 ºC	T_i
7	OSL for 60 s at 280 ºC	-

Supplementary figures

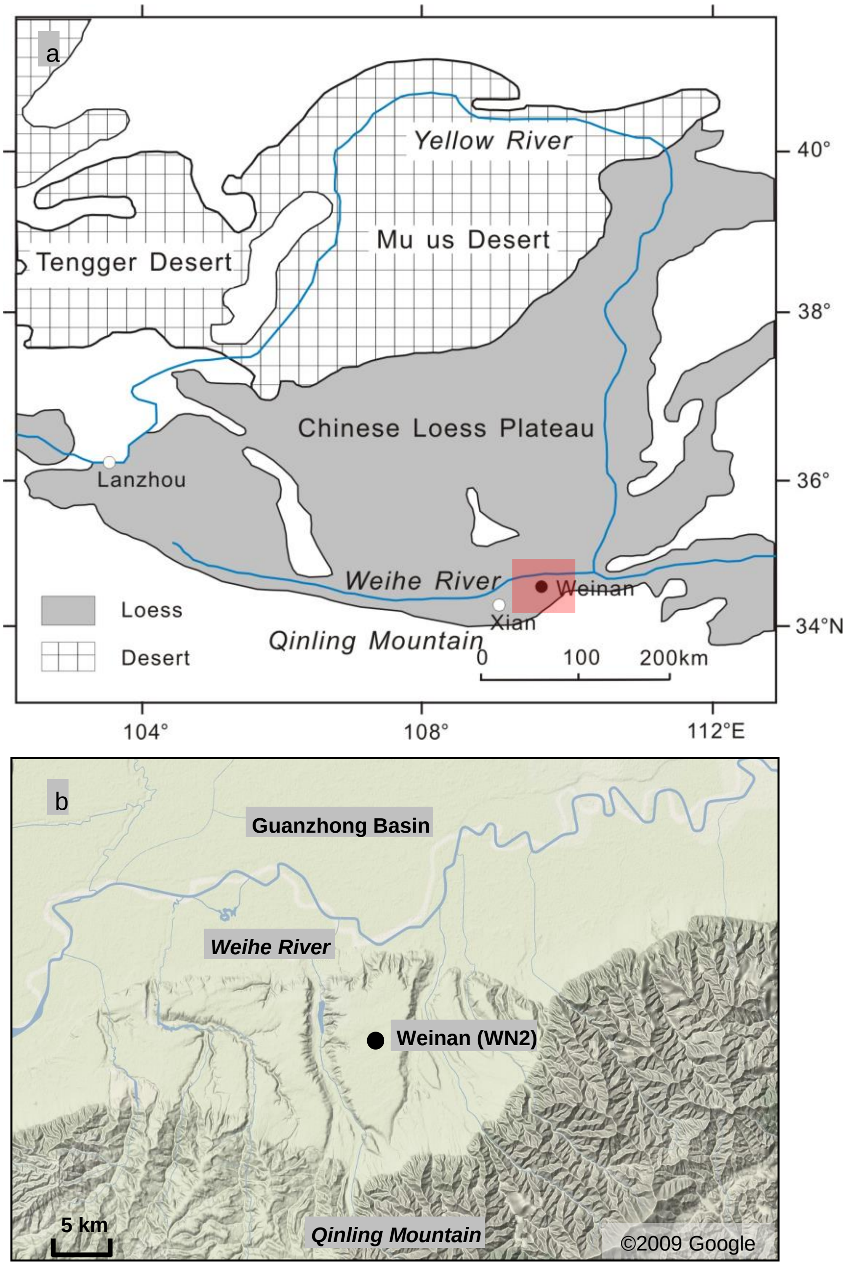

Figure S1 Location and regional geomorphology of the Weinan (WN2) site on the Chinese Loess Plateau (CLP). (a) Map showing the study site of WN2 (black circle) and the main body of the CLP (grey area), drawn using Excel2003 and CorelDraw12. The area in the red rectangle is identical to that in (b). (b) Regional geomorphology around the WN2 loess section, redrawn from Google (https://www.google.com/maps).

Kang, S., Wang, X.L., Roberts, H.M., Duller, G.A.T., Cheng, P., Lu, Y.C., and An, Z.S. (In Press, 2018) Late Holocene anti-phase change in the East Asian summer and winter monsoons. Quaternary Science Reviews
DOI: 10.1016/j.quascirev.2018.03.028

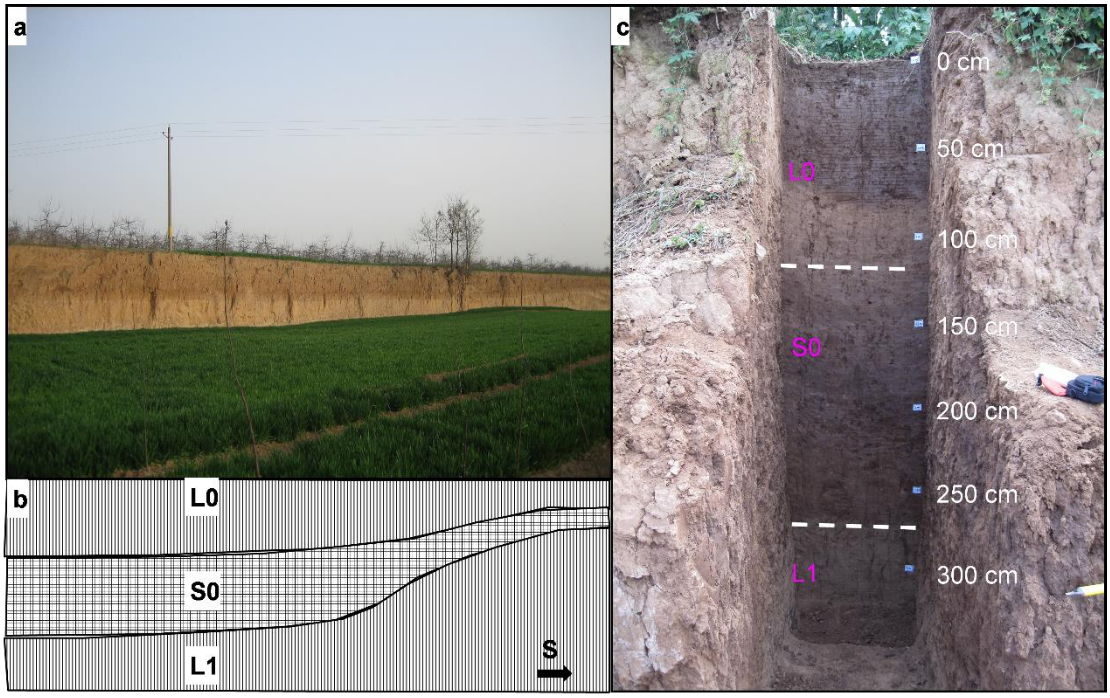

Figure S2 Weinan Holocene loess section outcrop, sketch of local geomorphology and sampling pit. (a) Late Last Glacial and Holocene loess outcrop created in a brickyard years ago. This picture is obtained in winter. (b) Sketch of the Weinan loess outcrop in (a), with L0, S0 and L1 indicate the late Holocene loess (or weakly developed palaeosol), the early-middle Holocene strongly developed palaeosol and the late Last Glacial loess. (c) Sampling pit, with depth and stratigraphic division also shown. This picture is obtained in summer. The letters L0, S0 and L1 are the same as those shown in (b). Note that the loess color above the depth of 60 cm in (c) is caused by heavy rainfall, days before sampling.

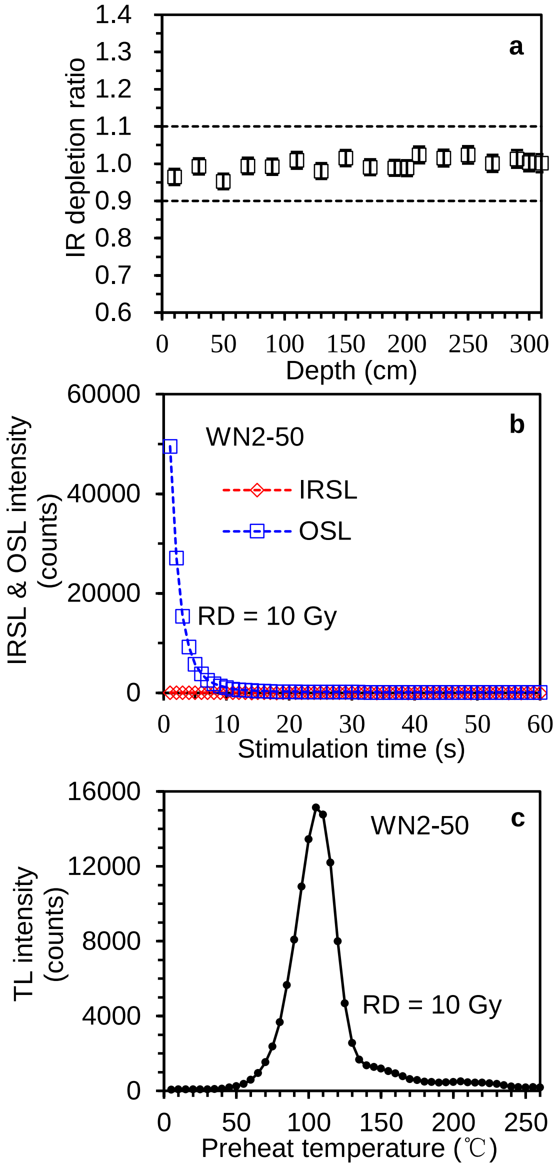

Figure S3 Fine-grained quartz purity tests of luminescence samples from the Weinan section. (a) OSL infrared (IR) depletion ratios (Duller, 2003), plotted against depth for all the 19 samples. (b) Regenerative dose (10 Gy) infrared stimulated luminescence (IRSL) and OSL decay curves of a typical sample WN2-50. (c) Regenerative dose (10 Gy) thermoluminescence (TL) glow curve of sample WN2-50. Data in (b) and (c) was derived after the measurement of natural OSL signal using the procedure in Table S1.

DOI: 10.1016/j.quascirev.2018.03.028

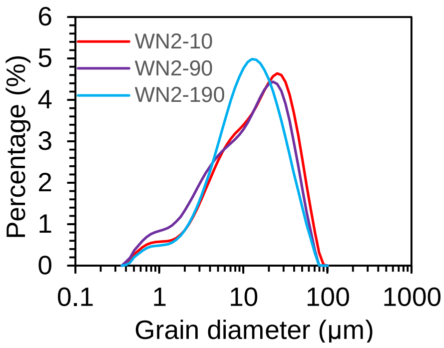

Figure S4 Grain size distribution of three typical samples (WN2-10, WN2-90 and WN2-190) from the late Holocene loess at Weinan, presented as volume percentage.

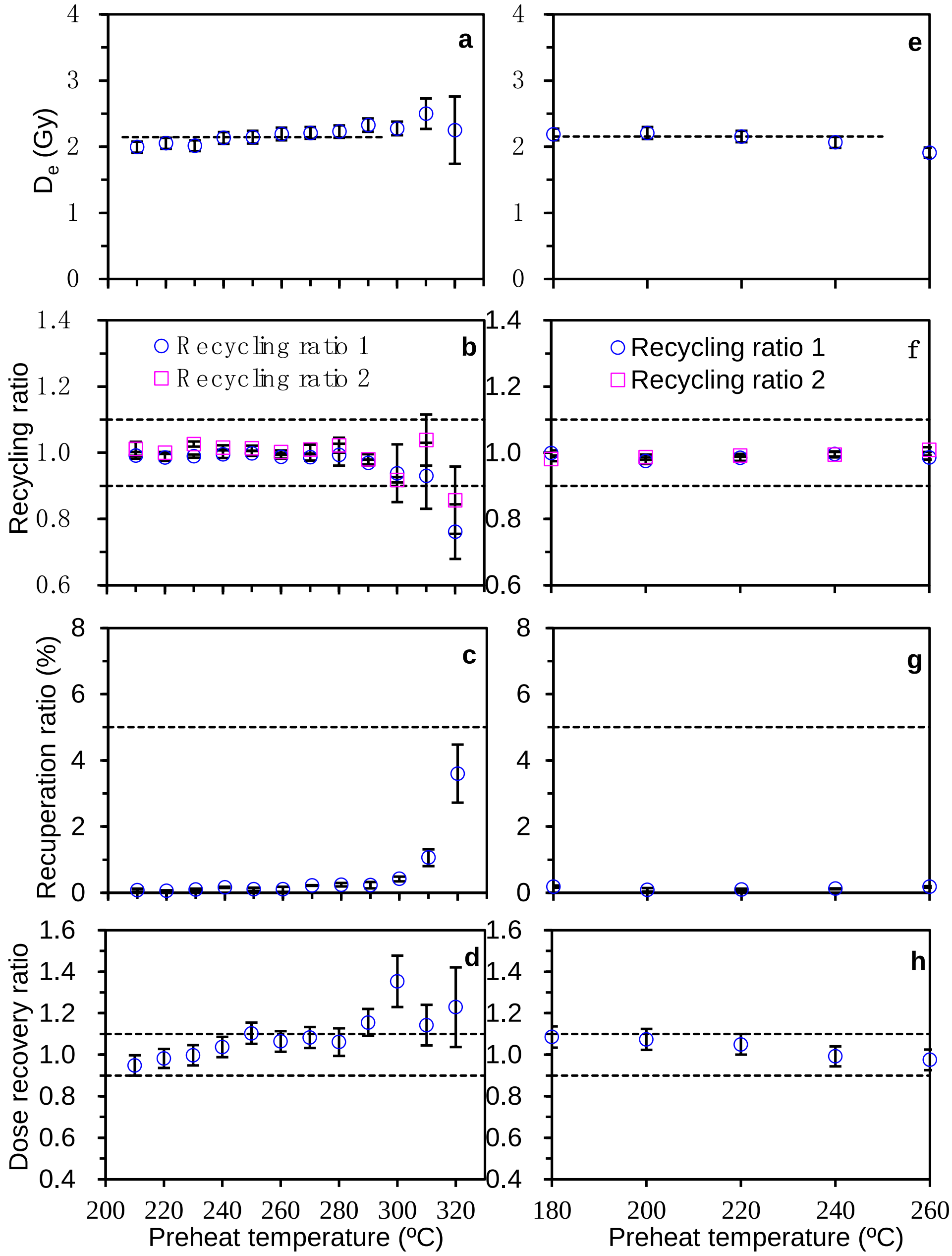

Figure S5 Equivalent dose (D_e) preheat plateau test for natural/regenerative dose (a-d) and test dose (e-h) of sample WN2-50 from Weinan. The test dose preheat temperature was fixed at 220 ºC for 10 s in (a-d) and the natural/regenerative-dose preheat temperature was fixed at 260 ºC for 10 s in (e-h). The dashed lines in (a) and (e) show the mean D_e values for natural/regenerative-dose preheat temperature spanning 210-290 ºC and for test dose preheat temperature spanning 180-240ºC, respectively. The recycling ratios (repeated/regenerated), recuperation ratios (recuperated/natural) and dose recovery ratios (measured/given) in natural/regenerative dose preheat plateau test are plotted in (b), (c) and (d), respectively, and those in test dose preheat plateau test are plotted in (f), (g) and (h), respectively.

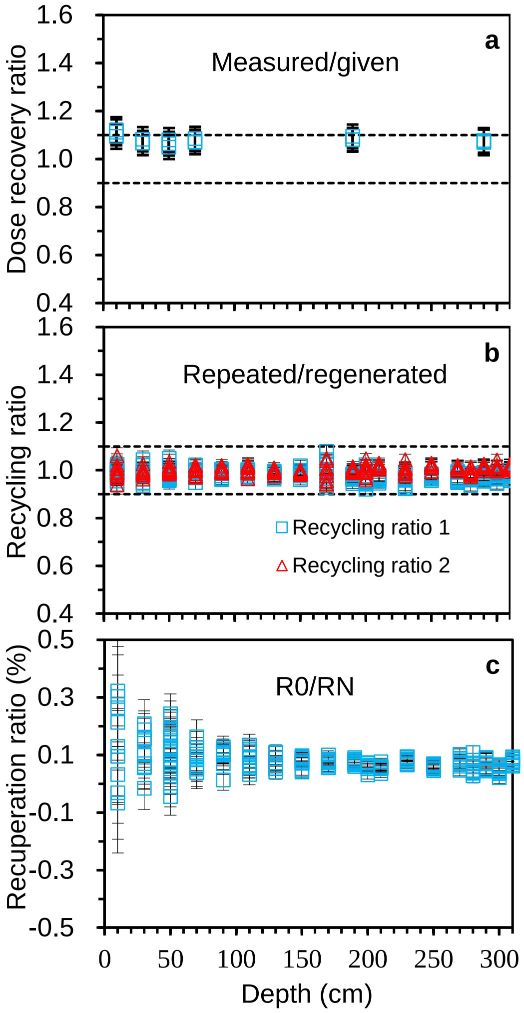

Figure S6 Dose recovery ratios (measured/given) for the six selected samples, WN2-10, WN2-30, WN2-50, WN2-70, WN2-190 and WN2-290 (a), and recycling ratios (repeated/regenerated) (b) and recuperation ratios (R0/RN) (c) for all of the 19 luminescence samples from Weinan in this study.

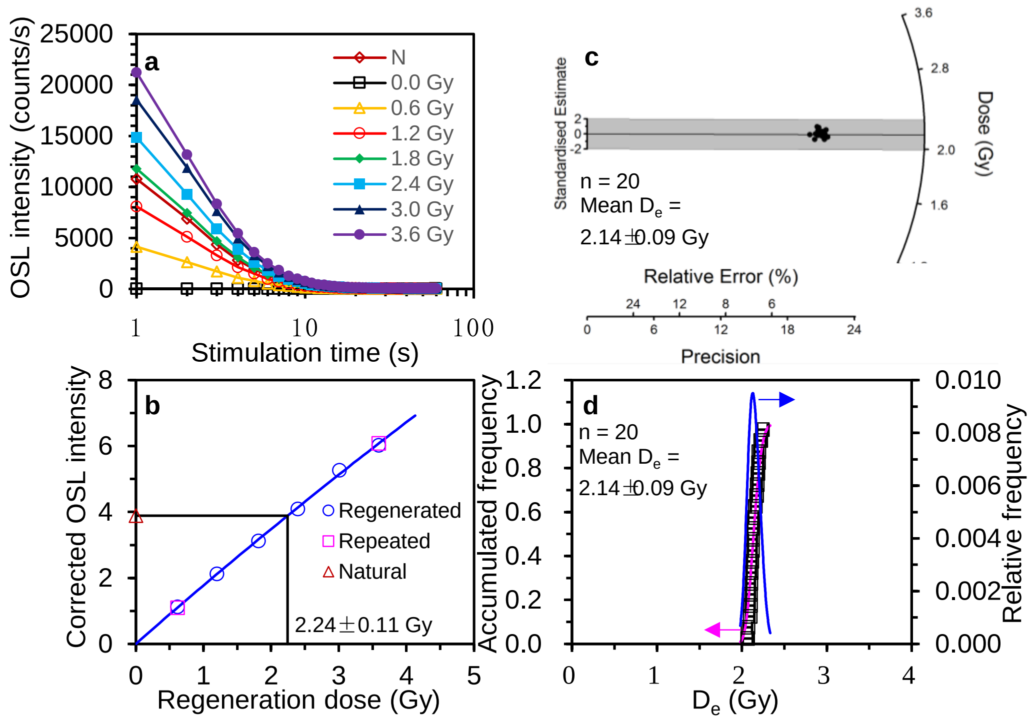

Figure S7 Equivalent dose (D_e) determination of sample WN2-50. (a) Natural and regenerative-dose OSL decay curves from a typical aliquot. Note that the x-axis is plotted as a log scale. (b) Dose-response curve and D_e determination derived from a typical aliquot. Sum of a constant and a saturated exponential was fitted to the regenerative-dose corrected OSL intensities. (c) D_e distribution presented in a radial plot. (d) Probability density distribution of D_e.

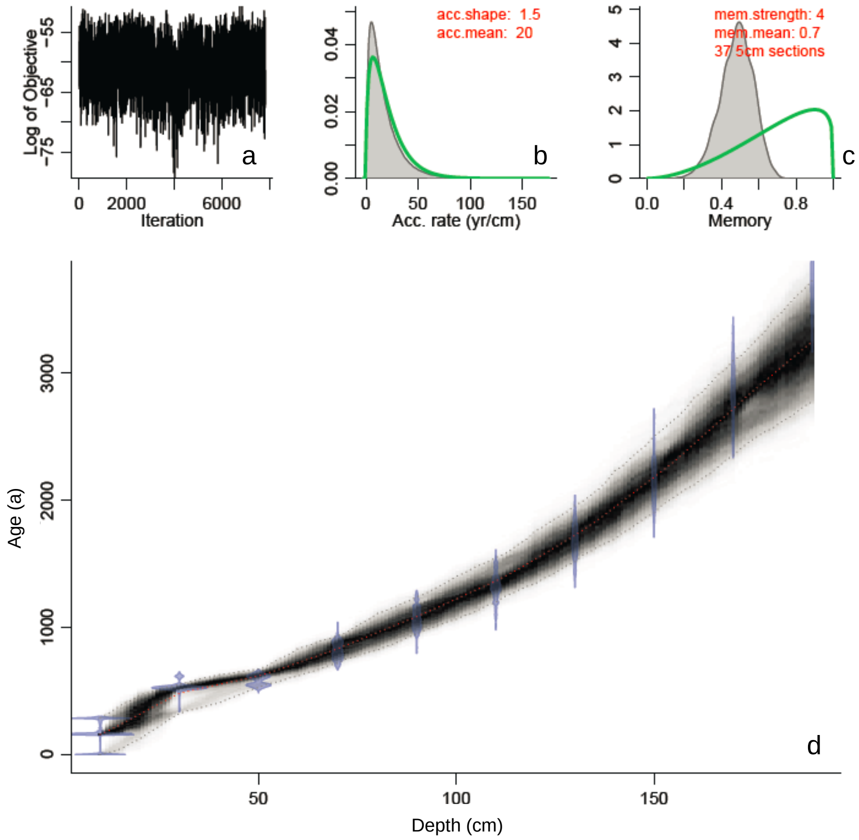

Figure S8 Bacon (Blaauw and Christen, 2011) output graph based on the Weinan late Holocene 10 quartz OSL ages (Table 1 and Fig. 3c). Upper panels depict the Markov Chain Monte Carlo (MCMC) iterations (a), the prior (green curves) and posterior (grey histograms) distributions for the accumulation rate (b) and memory (c). Bottom panel (d) shows the quartz OSL dates (transparent blue) and the age-depth model (darker greys indicate more likely ages; grey stippled lines show 95% confidence intervals; red curve shows single 'best' model based on the weighted mean age for each depth, adopted in this study).

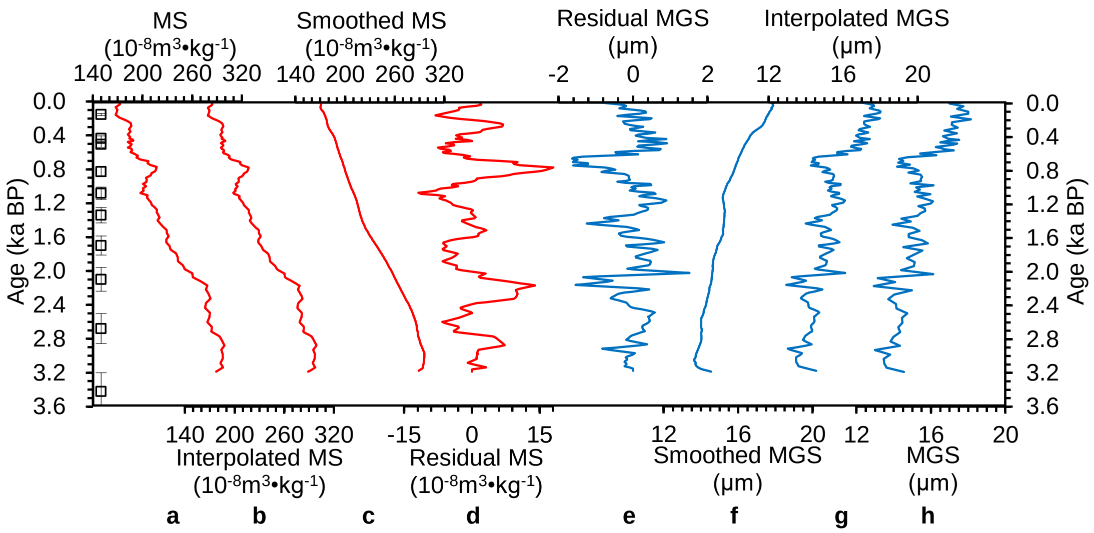

Figure S9 Measured magnetic susceptibility (MS) (a) and mean grain size (MGS) (h), same as those in Fig. 5, 250-point interpolated MS (b) and MGS (g), 1-ka (77 points) smoothed MS (c) and MGS (f), and residual MS (Δ MS) (d) and MGS (Δ MGS) (e), same as those in Figs. 6 and S11. OSL ages (corrected to ka BP) are also shown in (a). Note that the 1-ka smoothed data in (c) and (f) are based on the 250-point interpolated data in (b) and (g). Original numerical data in this figure can be found in Supplementary Data.

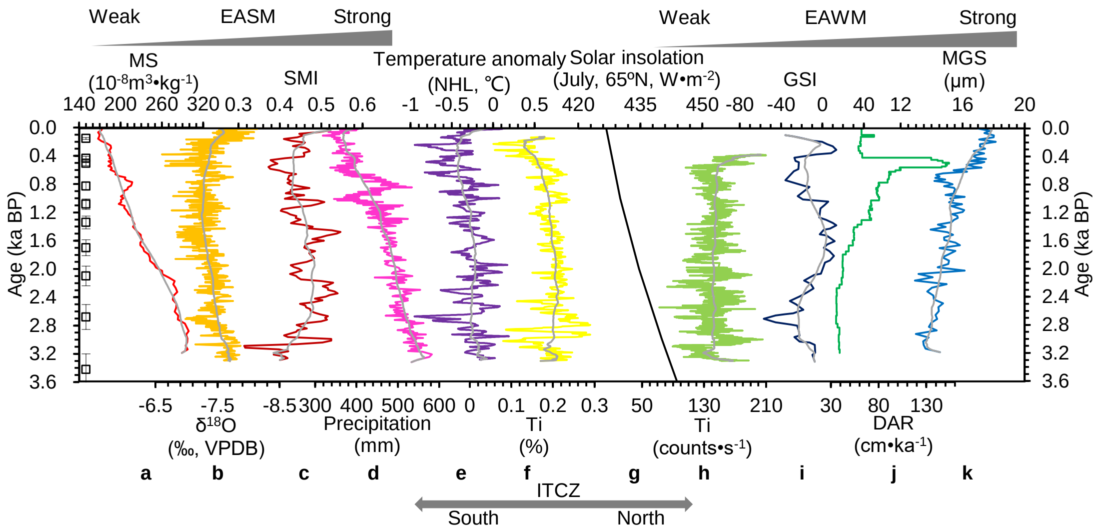

Figure S10 Same as Fig. 5, but with 1-ka smoothed lines indicated except in (g) and (j). Original numerical data in this figure can be found in Supplementary Data.

Kang, S., Wang, X.L., Roberts, H.M., Duller, G.A.T., Cheng, P., Lu, Y.C., and An, Z.S. (In Press, 2018) Late Holocene anti-phase change in the East Asian summer and winter monsoons. Quaternary Science Reviews
DOI: 10.1016/j.quascirev.2018.03.028

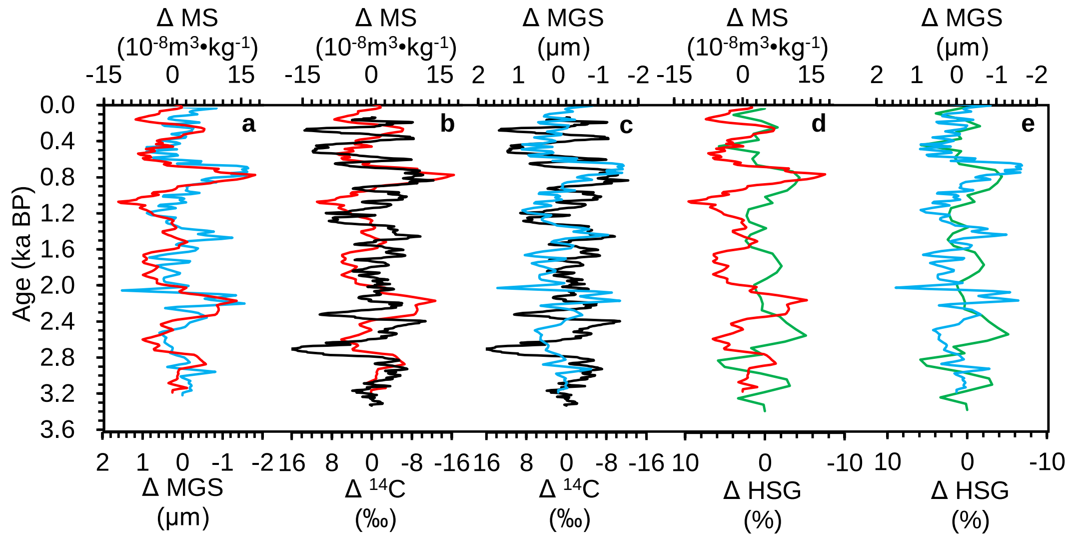

Figure S11 Comparisons of residual magnetic susceptibility (Δ MS, red) with residual mean grain size (Δ MGS, blue) of Weinan loess (a), Δ MS with atmospheric residual ^{14}C (Reimer et al., 2013) (Δ ^{14}C, black) (b), Δ MGS with atmospheric Δ^{14}C (Reimer et al., 2013) (c), Δ MS with North Atlantic residual Hematite-stained grains content (Bond et al., 2001) (Δ %HSG, green) (d) and Δ MGS with Δ %HSG (Bond et al., 2001). The curves presented here are the same with those in Figs. 6, S9 and S10, with long-term (larger than 1 ka) variations all removed. Original numerical data in this figure can be found in Supplementary Data.

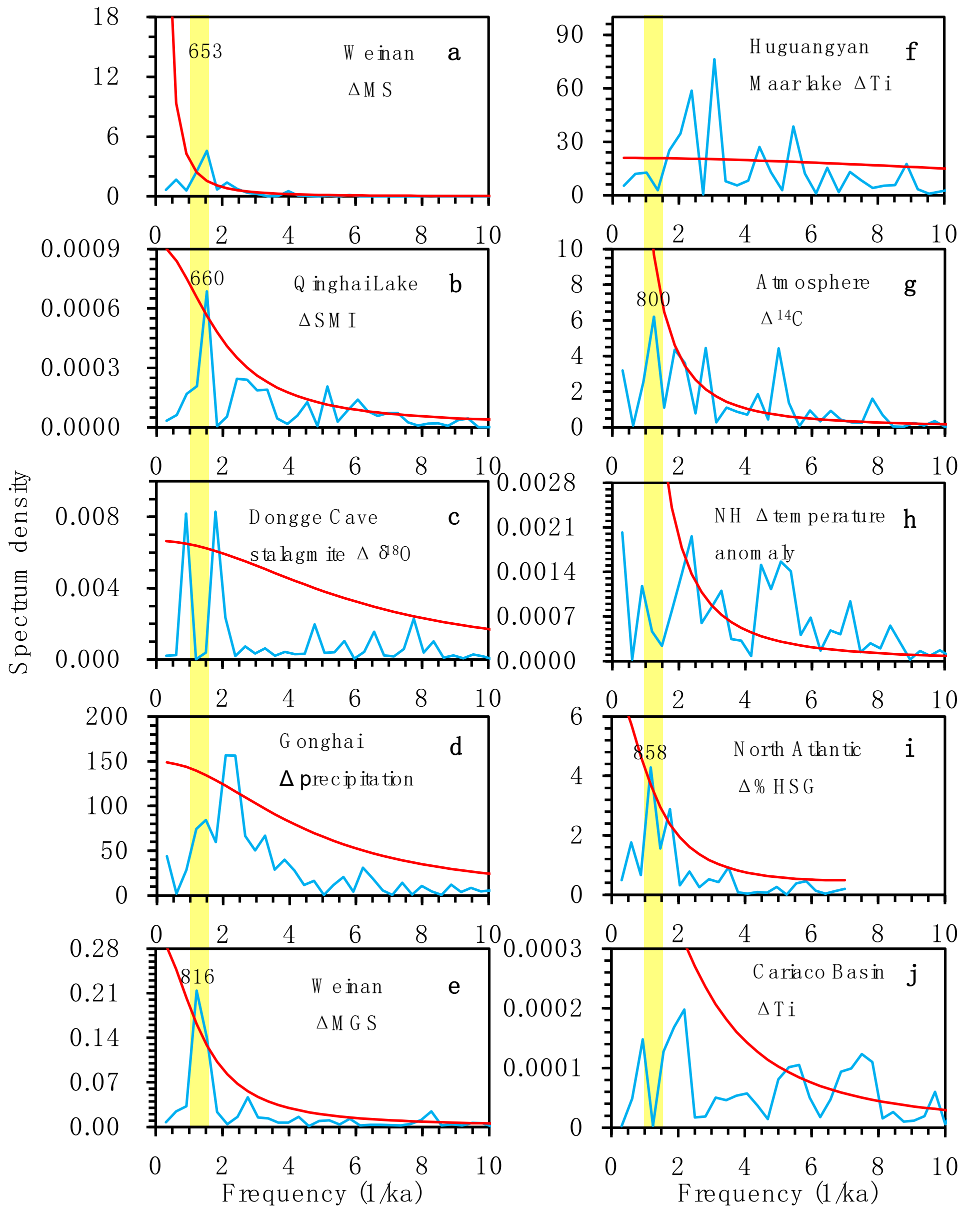

Figure S12 Periodicity analysis of Weinan loess magnetic susceptibility (Δ MS) (this study) (a), Qinghai Lake Asian summer monsoon index (Δ SMI) (An et al., 2012) (b), Dongge Cave stalagmite Δ δ^{18}O (Wang et al., 2005) (c), Gonghai Lake reconstructed precipitation (Δ precipitation) (Chen et al., 2015) (d), Weinan loess mean grain size (Δ MGS) (this study) (e), Huguangyan (HGY) Maar Lake residual Ti content (Δ Ti) (Yancheva et al., 2007) (f), atmospheric residual ^{14}C (Δ ^{14}C) (Reimer et al., 2013) (g), North Hemisphere residual temperature anomaly (Δ temperature anomaly) (Kobashi et al., 2013) (h), North Atlantic residual Hematite-stained grains content (Δ %HSG) (Bond et al., 2001) (i) and Cariaco Basin residual Ti content (Δ Ti) (Haug et al., 2001) (j). The blue curve indicates the spectrum density, and the red one indicates the 90% confidence level in each figure. The yellow vertical bands were placed according to the most significant cycle in Δ MS (653 yr) Δ MGS (816 yr), Δ ^{14}C (800 yr) and Δ %HSG (858 yr). Only frequency lower than 10, equal to 100 yr, was plotted here. Original numerical data in this figure can be found in Supplementary Data.

Supplementary references

An, Z.S., Colman, S.M., Zhou, W.J., Li, X.Q., Brown, E.T., Jull, A.J.T., Cai, Y.J., Huang, Y.S., Lu, X.F., Chang, H., Song, Y.G., Sun, Y.B., Xu, H., Liu, W.G., Jin, Z.D., Liu, X.D., Cheng, P., Liu, Y., Ai, L., Li, X.Z., Liu, X.J., Yan, L.B., Shi, Z.G., Wang, X.L., Wu, F., Qiang, X.K., Dong, J.B., Lu, F.Y., Xu, X.W., 2012. Interplay between the Westerlies and Asian monsoon recorded in Lake Qinghai sediments since 32 ka. Sci Rep 2, 619.

Blaauw, M., Christen, J.A., 2011. Flexible paleoclimate age-depth models using an autoregressive gamma process. Bayesian Analysis 6, 457-474.

Bond, G., Kromer, B., Beer, J., Muscheler, R., Evans, M.N., Showers, W., Hoffmann, S., Lotti-Bond, R., Hajdas, I., Bonani, G., 2001. Persistent solar influence on North Atlantic climate during the Holocene. Science 294, 2130-2136.

Chen, F., Xu, Q., Chen, J., Birks, H.J.B., Liu, J., Zhang, S., Jin, L., An, C., Telford, R.J., Cao, X., Wang, Z., Zhang, X., Selvaraj, K., Lu, H., Li, Y., Zheng, Z., Wang, H., Zhou, A., Dong, G., Zhang, J., Huang, X., Bloemendal, J., Rao, Z., 2015. East Asian summer monsoon precipitation variability since the last deglaciation. Sci Rep 5, 11186.

Duller, G., 2003. Distinguishing quartz and feldspar in single grain luminescence measurements. Radiat Meas 37, 161-165.

Duller, G.A.T., 2007. Assessing the error on equivalent dose estimates derived from single aliquot regenerative dose measurements. Ancient TL 25, 15-24.

Haug, G.H., Hughen, K.A., Sigman, D.M., Peterson, L.C., Röhl, U., 2001. Southward migration of the intertropical convergence zone through the Holocene. Science 293, 1304-1308.

Kobashi, T., Goto-Azuma, K., Box, J., Gao, C.-C., Nakaegawa, T., 2013. Causes of Greenland temperature variability over the past 4000 yr: implications for northern hemispheric temperature changes. Clim. Past. 9, 2299-2317.

Murray, A.S., Wintle, A.G., 2000. Luminescence dating of quartz using an improved single-aliquot regenerative-dose protocol. Radiat Meas 32, 57-73.

Reimer, P.J., Bard, E., Bayliss, A., Beck, J.W., Blackwell, P.G., Bronk Ramsey, C., Buck, C.E., Cheng, H., Edwards, R.L., Friedrich, M., 2013. IntCal13 and Marine13 radiocarbon age calibration curves 0-50,000 years cal BP. Radiocarbon 55, 1869-1887.

Schulz, M., Mudelsee, M., 2002. REDFIT: estimating red-noise spectra directly from unevenly spaced paleoclimatic time series. Computers & Geosciences 28, 421-426.

Wang, Y., Cheng, H., Edwards, R.L., He, Y., Kong, X., An, Z., Wu, J., Kelly, M.J., Dykoski, C.A., Li, X., 2005. The Holocene Asian monsoon: links to solar changes and North Atlantic climate. Science 308, 854-857.

Wintle, A.G., Murray, A.S., 2006. A review of quartz optically stimulated luminescence characteristics and their relevance in single-aliquot regeneration dating protocols. Radiat Meas 41, 369-391.

Yancheva, G., Nowaczyk, N.R., Mingram, J., Dulski, P., Schettler, G., Negendank, J.F.W., Liu, J., Sigman, D.M., Peterson, L.C., Haug, G.H., 2007. Influence of the intertropical convergence zone on the East Asian monsoon. Nature 445, 74-77.